ADVANCED FUNCTIONAL MATERIALS
www.afm-journal.de

Materials Views
www.MaterialsViews.com

# Iron Oxide Nanoparticle and Graphene Nanoribbon Composite as an Anode Material for High-Performance Li-Ion Batteries

*Jian Lin, Abdul-Rahman O. Raji, Kewang Nan, Zhiwei Peng, Zheng Yan, Errol L. G. Samuel, Douglas Natelson,* and James M. Tour**

**A composite material made of graphene nanoribbons and iron oxide nanoparticles provides a remarkable route to lithium-ion battery anode with high specific capacity and cycle stability. At a rate of 100 mA/g, the material exhibits a high discharge capacity of ~910 mAh/g after 134 cycles, which is >90% of the theoretical li-ion storage capacity of iron oxide. Carbon black, carbon nanotubes, and graphene flakes have been employed by researchers to achieve conductivity and stability in lithium-ion electrode materials. Herein, the use of graphene nanoribbons as a conductive platform on which iron oxide nanoparticles are formed combines the advantages of long carbon nanotubes and flat graphene surfaces. The high capacity over prolonged cycling achieved is due to the synergy between an electrically percolating networks of conductive graphene nanoribbons and the high lithium-ion storage capability of iron oxide nanoparticles.**

## 1. Introduction

The advancement of environmentally acceptable anode materials for lithium-ion batteries (LIBs) with high energy and power density and a long life-time is a key step for the development of large-scale applications for portable electronics, renewable energy source and electrical vehicles.[1,2] To this end, iron oxide as an anode material for LIBs has drawn much attention because of its large reversible capacity (~1007 mAh/g), low cost, and non-toxicity.[3–6] However, the poor intrinsic electrical conductivity and large capacity decay caused by the large volume expansion of iron oxide during lithiation hinder its practical applications for LIBs. There are different approaches to overcome these problems; one solution is to fabricate iron oxide nanostructures such as nanoparticles (NPs),[3,7] nanoribbons[6] and nanorods.[8] Other solutions are to confine the iron oxide nanostructures with carbon[9–12] or to form a composite of the iron oxide with the carbon host matrix such that the carbon host acts as a mechanical buffer to release strain during cycling and to enhance lithium diffusion into the electrode.[4,5,13] Thus, the electrochemical performance of iron oxide-based anode has been significantly improved.

Quasi 1D graphene nanoribbons (GNRs) with good electrical conductivity[14] and high aspect-ratio offer a suitable conductive matrix and provide mechanical flexibility for the iron oxide to accommodate volume changes during cycling. We demonstrate here a facile route to prepare a nanocomposite from GNRs and $Fe_2O_3$ NPs. GNRs were coated with ~10 nm $Fe_2O_3$ NPs. The as-prepared $Fe_2O_3$ NPs were predominately the maghemite phase ($\gamma$-$Fe_2O_3$). Fabricated electrodes made from the as-prepared nanocomposite exhibit an enhanced reversible capacity of >1100 mAh/g in the first 20 cycles and maintain >910 mAh/g after 134 cycles at a current density of 200 mA/g. The electrodes also have a high capacity performance of >540 mAh/g at a charging rate of 2 A/g, still much larger than the capacity of graphite (372 mAh/g). The superior electrochemical performance of the as-prepared nanocomposite can be attributed to the unique structure of the $Fe_2O_3$ NPs conformally coated with conductive GNRs.

## 2. Results and Discussion

**Figure 1**a illustrates the synthesis procedure of the GNR/$Fe_2O_3$ NPs composite. The GNRs were produced from unzipping multiwall carbon nanotubes (MWCNTs) that were treated with K/Na alloy, producing K-intercalated MWCNTs.[14–16] $FeCl_3$ was added and reduced by the K/Na to form Fe. This process partially split MWCNTs on which Fe NPs were coated. The Na/K

A.-R. O. Raji, Z. Peng, Z. Yan, E. L. G. Samuel, Prof. J. M. Tour
Department of Chemistry
Rice University
6100 Main St., Houston, Texas, 77005, USA
E-mail: tour@rice.edu
Prof. D. Natelson
Department of Physics and Astronomy
Rice University
6100 Main St., Houston, Texas, 77005, USA
E-mail: natelson@rice.edu
Dr. J. Lin, K. Nan, Prof. J. M. Tour
Department of Mechanical Engineering and Materials Science
Rice University
6100 Main St., Houston, Texas, 77005, USA
Dr. J. Lin, Prof. D. Natelson, Prof. J. M. Tour
Smalley Institute for Nanoscale Science & Technology
Rice University
6100 Main St., Houston, Texas, 77005, USA

**DOI: 10.1002/adfm.201303023**

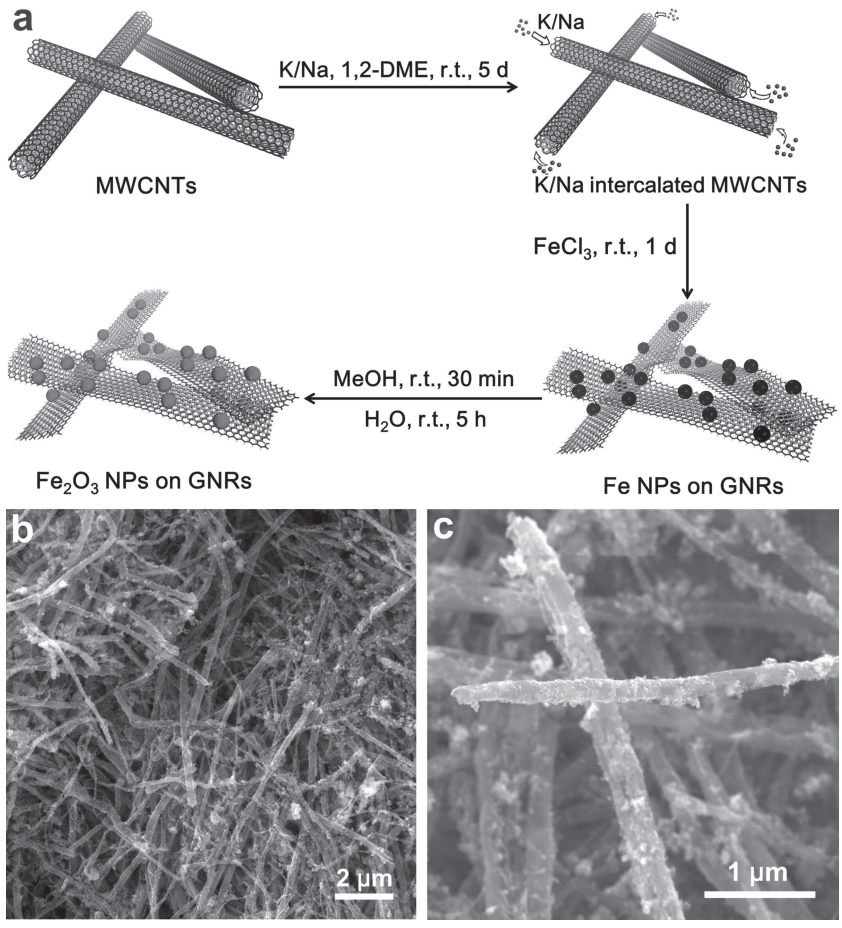


**Figure 1.** a) Scheme of the synthesis of the GNR/$Fe_2O_3$ composites. b) Low magnification SEM image of the GNR/$Fe_2O_3$-P composites. c) High magnification SEM image of the GNR/$Fe_2O_3$-P composites.

alloy was quenched with $CH_3OH$, generating $H_2$ that induced efficient unzipping of the MWCNTs into GNRs. In the above procedures, generated impurities such as KCl, NaCl, $CH_3OK$ and $CH_3OH$ are water-soluble and were removed during washing. Next, the obtained GNRs/Fe composite was washed with deionized water, oxidizing the Fe NPs to iron oxide NPs, or GNR/$Fe_2O_3$-P where "P" stands for pre-annealing (for details, see the Supporting Information). Subsequently, the composite was annealed in air at 250 or 300 °C for 14 h. The samples were denoted as GNR/$Fe_2O_3$-250 and GNR/$Fe_2O_3$-300, respectively. The morphology of the GNR/$Fe_2O_3$-P is shown in Figure 1b, in which the well dispersed GNRs, with widths of ~200 nm and lengths up to a 100 μm, form an interconnected web as observed with field emission scanning electron microscopy (SEM). The enlarged SEM image in Figure 1c shows that the GNRs are well covered by $Fe_2O_3$ NPs. This structure facilitates charge transfer between the $Fe_2O_3$ NPs and the current collectors.

To analyze the crystal structure of the GNR/$Fe_2O_3$-P, GNR/$Fe_2O_3$-250, and GNR/$Fe_2O_3$-300, X-ray diffraction (XRD) measurements were performed (**Figure 2**). The characteristic peak at $2\theta = 26.3°$ confirms the existence of graphene layers in all of the composites. Furthermore, the as-prepared composite shows a predominance of the maghemite phase of iron oxide (γ-$Fe_2O_3$). From XRD analyses, when annealed at 250 °C for 14 h, the more stable hematite iron oxide (α-$Fe_2O_3$) begins to appear in the GNR/$Fe_2O_3$-250. As the annealing temperature was increased to 300 °C, the stronger characteristic peaks of the hematite phase appeared, indicating the higher concentration of α-$Fe_2O_3$ in the GNR/$Fe_2O_3$-300. The different phases of the composites greatly impact the electrochemical performance.

The morphology and crystal structure of the composite were also investigated by transmission electron microscopy (TEM, **Figure 3**). Figure 3a, taken from GNR/$Fe_2O_3$-P, shows well-distributed $Fe_2O_3$ NPs along the GNRs. Figure 3b shows that the sizes of the NPs are ~10 nm and the lattice spacing between graphene layers is 0.34 nm. Further inspection of the γ-$Fe_2O_3$ by high resolution TEM (HRTEM) shows different domains with clearly observed lattice fringes in each domain (Figures 3c), indicative of the polycrystalline nature of the as-prepared γ-$Fe_2O_3$ NPs. The uniform distance between the lattice fringes is 0.25 nm, in good agreement with the spacing between (311) planes of γ-$Fe_2O_3$. Normally, the synthesis of γ-$Fe_2O_3$ involves an aqueous pathway that results in metal cation vacancies induced by the water being incorporated into the material.[17,18] When annealed at 250 °C or higher, some

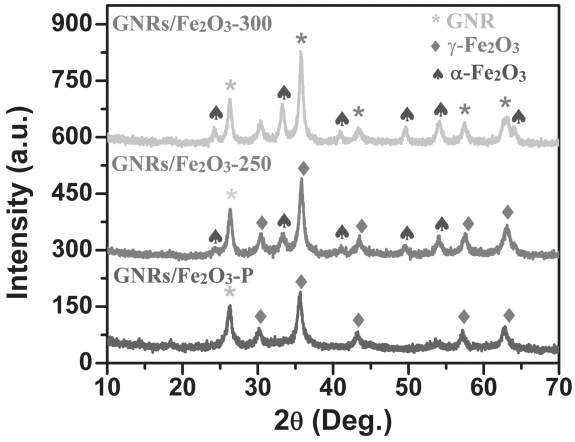


**Figure 2.** XRD spectrum of GNR/$Fe_2O_3$ composite at different annealing temperatures. Bottom: The sample GNR/$Fe_2O_3$-P shows a predominance of the maghemite phase of iron oxide (γ-$Fe_2O_3$). Middle: Annealed at 250 °C, hematite iron oxide (α-$Fe_2O_3$) appears in the GNR/$Fe_2O_3$-250. Top: As the annealing temperature increased to 300 °C, the stronger characteristic peaks of hematite phase indicate the higher concentration of α-$Fe_2O_3$ in the GNR/$Fe_2O_3$-300.

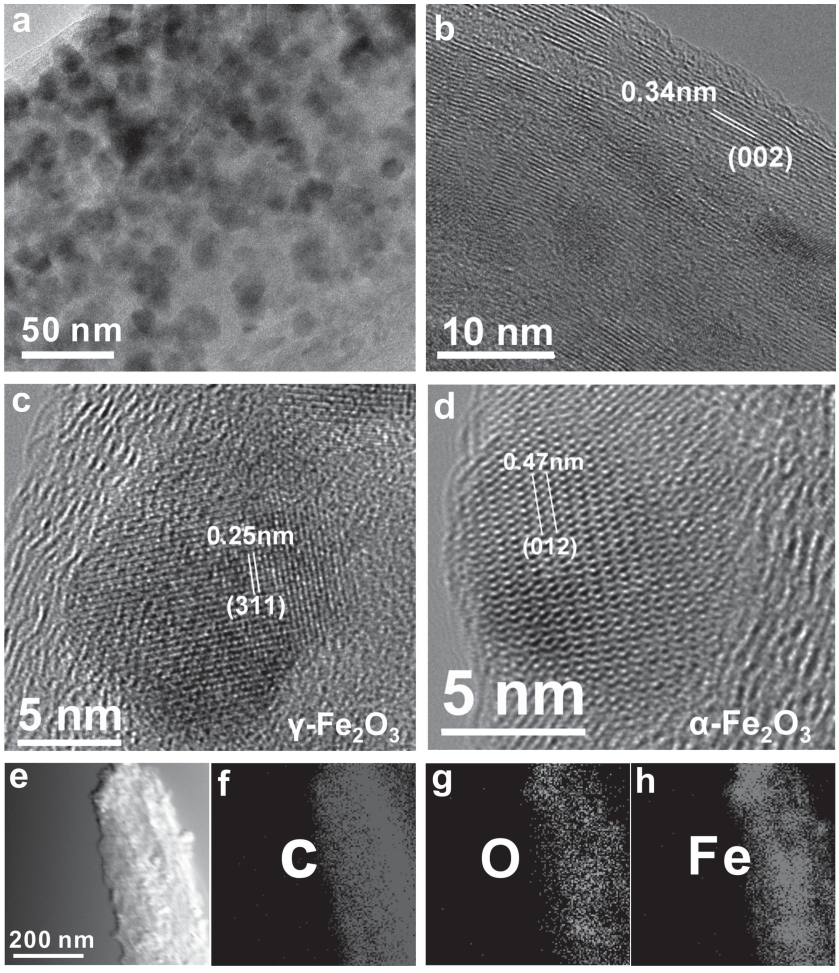


**Figure 3.** TEM characterizations of GNR/$Fe_2O_3$ composite. a) TEM image of synthesized GNR/$Fe_2O_3$ composite showing uniformly distributed $Fe_2O_3$ NPs on GNRs. b) HRTEM image showing graphite structure of GNRs. c) HRTEM image of a representative γ-$Fe_2O_3$ NP. The well-defined diffraction pattern indicates the high crystallinity of γ-$Fe_2O_3$ NPs. d) HRTEM image of a representative α-$Fe_2O_3$ NP. e) An STEM image of the GNR/$Fe_2O_3$ composite and the corresponding elemental mapping of f) carbon, g) oxygen and h) iron, suggesting the homogeneous dispersion of C, O and Fe in the composites.

of the γ-$Fe_2O_3$ NPs are converted to more thermodynamically stable α-$Fe_2O_3$,[19] as shown in Figure 2d taken from GNR/$Fe_2O_3$-250. The distance of 0.47 nm between the uniform lattice fringe is the spacing of plane $Fe_2O_3$ (012). To confirm the composition of GNR/$Fe_2O_3$, a TEM elemental mapping by was performed. As shown in Figure 2e–h, carbon, oxygen and iron were homogeneously distributed in the GNRs.

To gain further insight into the composite, X-ray photoelectron spectroscopy (XPS, Figure S1) was done on GNR/$Fe_2O_3$-P. Carbon, oxygen and iron were detected in the XPS spectrum, (Figure S1), consistent with the result from the elemental mapping. The XPS atomic percentage of 54.8% for carbon corresponds to 36.6 wt% carbon. This result is consistent with the thermogravimetric analysis data (TGA, Figure S2). The Raman spectrum of the GNR/$Fe_2O_3$-P reveals strong peaks at 223 ($A_{1g}$), 290 ($E_g$), 408 ($E_g$), and 1321 $cm^{-1}$, a weaker peak at 607 ($E_g$) $cm^{-1}$, and very weak peaks at 242 ($E_g$) and 497 ($A_{1g}$) $cm^{-1}$ (Figure S3). These vibrational modes are in good agreement with the characteristic peaks of α-$Fe_2O_3$.[20] The broad peak at 660 $cm^{-1}$ could be attributed to the maghemite residues in the sample.[20] The reason for this major α-phase result by Raman when the XRD pattern of the GNR/$Fe_2O_3$-P showed a predominance of the γ-phase (Figure 2), could be because α-$Fe_2O_3$ has a larger Raman cross-section than γ-$Fe_2O_3$ as previously suggested.[20] Another reason could be the induced irreversible transformation to the α-phase by laser power.[21]

The electrochemical lithium storage properties of the GNR/$Fe_2O_3$ composites as anode materials for LIBs were investigated by cyclic voltammetry (CV) measurements, galvanostatic charge/discharge measurements and electrochemical impedance spectroscopy measurements. **Figure 4**a shows the CV curves of an electrode made from GNR/$Fe_2O_3$-P. The CV curves of the initial three cycles were obtained from 0.01 V to 3 V at a scan rate of 0.5 mV/s. In the first cycle, unlike the ordinary α-$Fe_2O_3$ electrode, there are no peaks at 1.0 V and only a minuscule peak at 1.5 V,[5] both of which correspond to the formation of hexagonal α-$Li_xFe_2O_3$ and phase change from α-$Li_xFe_2O_3$ to cubic $Li_xFe_2O_3$. This result agrees with the XRD result, suggesting that the predominant phase of the iron oxide NPs is maghemite (γ-$Fe_2O_3$). The profound cathodic peak at 0.5 V corresponds to the formation of a solid electrolyte interface (SEI) and the complete reduction to Fe(0). This peak disappears in subsequent cycles and evolves into a peak at 0.73 V, which is thought to be the reversible lithium insertion and complete reduction of FeO to Fe(0).[5,13] The broad anodic peak at ~1.8 V corresponds to the reversible oxidization of Fe(0) to Fe(III). The reproducible cathodic and anodic peaks at 0.73 V and 1.8 V, respectively, in the second and third cycles agree well with the plateau voltages in the galvanostatic charge-discharge curves at a current density of 100 mA/g, with a cut-off potential window of 0.01–3.0 V (Figure 4b). The composite electrodes deliver an initial discharge capacity of 1586 mAh/g, with a reversible charge capacity of 1117 mAh/g. The relatively low 29% irreversibility can be attributed to the formation of SEI or the decomposition of electrolyte, which is quite common in lithium-ion battery electrodes.[22–24] In the second cycle, the discharge and charge capacities of 1224 mAh/g and 1110 mAh/g indicate the high reversibility. The lithium storage capacity is more than the theoretical value of iron oxide (~1007 mAh/g). This enhanced storage capability occurs in some metal oxide nanostructures.[25–27] Recent solid-state NMR study reveals that the excessive lithium storage in metal oxides is due to the generation of LiOH and its subsequent reversible reaction with Li to form $Li_2O$ and LiH.[28]

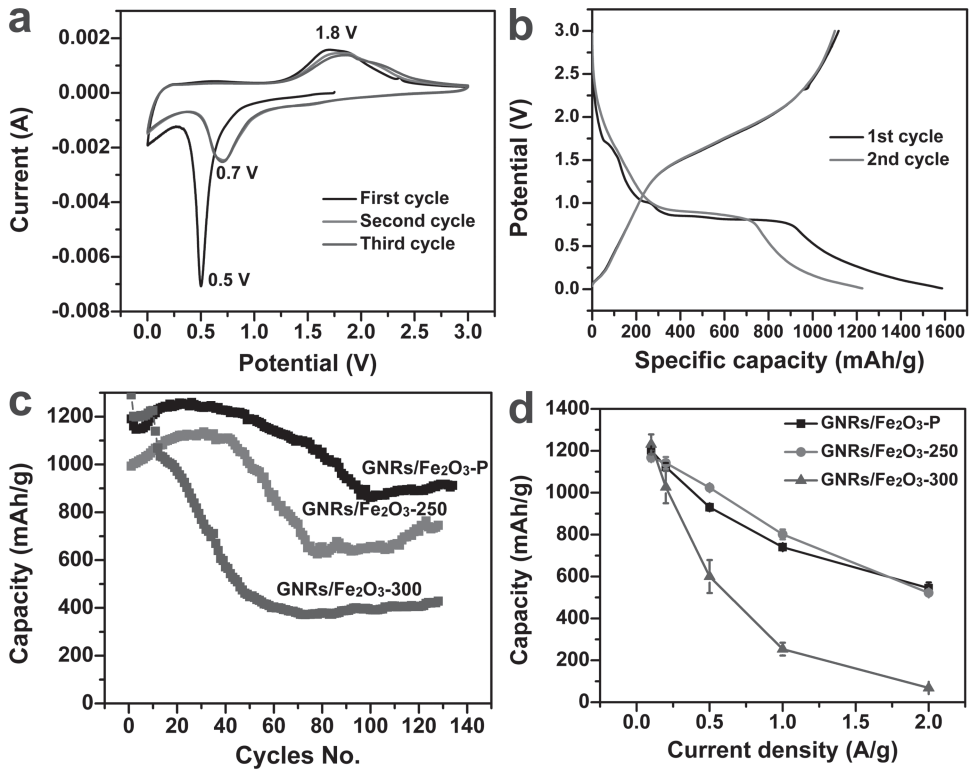


**Figure 4.** Electrochemical properties of GNR/$Fe_2O_3$ composite anode electrodes. All of the capacities shown here are based on the weight of iron oxide NPs. a) Cyclic voltammetry of the GNR/$Fe_2O_3$-P composite anode. b) The first and second charge-discharge curves of the composite GNR/$Fe_2O_3$-P anode. c) Comparison of the cyclability of GNR/$Fe_2O_3$-P, GNR/$Fe_2O_3$-250, and GNR/$Fe_2O_3$-300 at a rate of 0.2 A/g. d) Comparison of rate performance of GNR/$Fe_2O_3$-P, GNR/$Fe_2O_3$-250, and GNR/$Fe_2O_3$-300.

To further characterize the lithium storage properties of the composite electrodes with various annealing conditions, capacity retention tests were performed at a current density of 0.2 A/g (Figure 4c). The as-prepared GNR/$Fe_2O_3$-P electrodes exhibited an initial discharge capacity of 1190 mAh/g that increased to 1259 mAh/g after 26 cycles. Such capacity rise could be due to transformation of the crystalline structure to an amorphous-like structure during cycling, thus enhancing the lithium insertion kinetics.[29] In the following cycles the capacity was slowly decreased then stabilized at ~850 mAh/g after ~90 cycles. This stabilization can be attributed to the stably transformed phase and structure of the host materials. Finally, the capacity remained ~910 mAh/g after 134 cycles. However, when annealed at elevated temperature, the initial capacity is not only less than that in the as-prepared sample, but the capacity retention decays much faster. In the case of GNR/$Fe_2O_3$-250, the initial capacity was ~1003 mAh/g and was at ~745 mAh/g after 128 cycles. The electrodes prepared with GNR/$Fe_2O_3$-300 had an initial capacity of 1291 mAh/g. However, the capacity quickly decayed to ~400 mAh/g after 50 cycles. The decreased capacity could be due to a number of reasons. The polycrystalline structure of the as-prepared $Fe_2O_3$ NPs ($\gamma$-$Fe_2O_3$), containing cationic vacancies, could enhance lithium storage kinetics.[3,17,30] In addition, the $\gamma$-$Fe_2O_3$ phase of iron oxide does not possess the phase transition that $\alpha$-$Fe_2O_3$ has during lithium insertion; this phase transition induces irreversible lithium storage.[5] As the annealing temperature increased, the concentration of $\alpha$-$Fe_2O_3$ in the composite increased, leading to irreversible lithium storage. In addition, when annealed at 300 °C, GNR layers start to oxidize, thus losing electrical conductivity. To investigate the major contribution of the lithium storage capacity, control experiments were performed. Figure S4 shows the capacity retention of bare GNRs at a rate of 0.2 A/g. The low reversible capacity of ~245 mAh/g from bare GNRs suggests that the major contribution of lithium storage capacity is from iron oxide NPs. To demonstrate the superior performance of the GNR/$Fe_2O_3$ composite, the cycling performance of $Fe_2O_3$ NPs without GNRs at a current density of 0.2 A/g was investigated (Figure S5). The capacity quickly degraded to ~180 mAh/g after 50 cycles, indicative of the important role of GNRs in the cycling performance of the electrodes.

The rate capability is an important parameter in evaluating the lithium storage performance of the electrodes. Here, the GNRs/$Fe_2O_3$ composites prepared using different annealing conditions were investigated. Figure 4d compares the capacity performance when applying current densities from 0.1 A to 2 A. The representative cycling data at different current densities are shown in Figure S6. The rate capacity strongly depends on the annealing temperature. The GNR/$Fe_2O_3$-P shows high reversible capacity of 1201, 1123, 930, 740 and 544 mAh/g at current densities of 0.1, 0.2, 0.5, 1 and 2 A/g, respectively. And the GNR/$Fe_2O_3$-250 exhibits only slightly smaller capacities at

the same current densities, with a capacity of 520 mAh/g at a current density of 2 A/g. Furthermore, the reversible capacity for both GNR/$Fe_2O_3$-P and GNR/$Fe_2O_3$-250 can be recovered to the value close to the original value when the current density was returned to 0.1 A/g (Figure S6), indicative of the good rate performance. However, when the annealing temperature was increased to 300 °C, the rate performance was significantly degraded. The sample of GNRs/$Fe_2O_3$-300 shows a capacity of only 68 mAh/g at the current density of 2 A/g.

## 3. Conclusion

A facile and scalable synthesis route to GNR/$Fe_2O_3$ composite was developed. The as-prepared composite anode material for LIBs had a reversible capacity as high as 1190 mAh/g and retained ~910 mAh/g after 134 cycles at a rate of 0.2 A/g. In addition, the anode exhibited good rate performance of 544 mAh/g at a rate of 2 A/g. The unique structures of GNRs with high electrical conductivity and the enhanced vacancy of iron oxide NPs leads to excellent electrochemical performance. It is also noteworthy that the annealing conditions of the composite greatly impact the lithium storage performance. As the annealing temperature increased to 300 °C, both the cycling retention and rate capacity were significantly degraded. This straightforward, accessible method for preparation of anode materials for LIBs could pave the way to a new route for achieving high-performance energy storage devices.

## Supporting Information

Supporting Information is available from the Wiley Online Library or from the author.

## Acknowledgements

J. Lin and A.-R. O. Raji contributed equally to this work. Funding for this research was provided by Boeing, the AFOSR MURI (FA9550–12–1–0035), the AFOSR (FA9550–09–1–0581), Sandia National Laboratory (1100745) and the ONR MURI program (#00006766, N00014–09–1–1066).

Received: August 29, 2013
Revised: October 4, 2013
Published online: November 20, 2013

[1] M. Armand, J. M. Tarascon, *Nature* **2008**, *451*, 652.
[2] M. S. Whittingham, *Chem. Rev.* **2004**, *104*, 4271.
[3] B. Koo, H. Xiong, M. D. Slater, V. B. Prakapenka, M. Baasubramanian, P. Podsiadlo, C. S. Johnson, T. Rajh, E. V. Shevchenko, *Nano Lett.* **2012**, *12*, 2429.
[4] Y. Wu, Y. Wei, J. Wang, K. Jiang, S. Fan, *Nano Lett.* **2013**, *13*, 818.
[5] Z. Y. Wang, D. Y. Luan, S. Madhavi, Y. Hu, X. W. Lou, *Energy Environ. Sci.* **2012**, *5*, 5252.
[6] S. B. Yang, Y. Sun, L. Chen, Y. Hernandez, X. L. Feng, K. Mullen, *Sci. Rep.* **2012**, *2*.
[7] P. Poizot, S. Laruelle, S. Grugeon, L. Dupont, J. M. Tarascon, *Nature* **2000**, *407*, 496.
[8] C. Z. Wu, P. Yin, X. Zhu, C. Z. OuYang, Y. Xie, *J. Phys. Chem. B* **2006**, *110*, 17806.
[9] J. S. Zhou, H. H. Song, X. H. Chen, L. J. Zhi, S. Y. Yang, J. P. Huo, W. T. Yang, *Chem. Mater.* **2009**, *21*, 2935.
[10] E. Kang, Y. S. Jung, A. S. Cavanagh, G. H. Kim, S. M. George, A. C. Dillon, J. K. Kim, J. Lee, *Adv. Funct. Mater.* **2011**, *21*, 2430.
[11] W. M. Zhang, X. L. Wu, J. S. Hu, Y. G. Guo, L. J. Wan, *Adv. Funct. Mater.* **2008**, *18*, 3941.
[12] S. B. Yang, X. L. Feng, S. Ivanovici, K. Mullen, *Angew. Chem. Int. Ed.* **2010**, *49*, 8408.
[13] X. J. Zhu, Y. W. Zhu, S. Murali, M. D. Stollers, R. S. Ruoff, *ACS Nano* **2011**, *5*, 3333.
[14] D. V. Kosynkin, W. Lu, A. Sinitskii, G. Pera, Z. Z. Sun, J. M. Tour, *ACS Nano* **2011**, *5*, 968.
[15] D. V. Kosynkin, A. L. Higginbotham, A. Sinitskii, J. R. Lomeda, A. Dimiev, B. K. Price, J. M. Tour, *Nature* **2009**, *458*, 872.
[16] B. Genorio, W. Lu, A. M. Dimiev, Y. Zhu, A. R. O. Raji, B. Novosel, L. B. Alemany, J. M. Tour, *ACS Nano* **2012**, *6*, 4231.
[17] B. P. Hahn, J. W. Long, A. N. Mansour, K. A. Pettigrew, M. S. Osofsky, D. R. Rolison, *Energy Environ. Sci.* **2011**, *4*, 1495.
[18] S. Laurent, D. Forge, M. Port, A. Roch, C. Robic, L. V. Elst, R. N. Muller, *Chem. Rev.* **2008**, *108*, 2064.
[19] I. David, A. J. E. Welch, *Trans. Faraday Soc.* **1956**, *52*, 1642.
[20] A. M. Jubb, H. C. Allen, *ACS Appl. Mater. Interfaces* **2010**, *2*, 2804.
[21] D. Bersani, P. P. Lottici, A. Montenero, *J. Raman Spectroscopy* **1999**, *30*, 355.
[22] L. F. Cui, Y. Yang, C. M. Hsu, Y. Cui, *Nano Lett.* **2009**, *9*, 3370.
[23] Y. Yao, K. F. Huo, L. B. Hu, N. A. Liu, J. J. Ha, M. T. McDowell, P. K. Chu, Y. Cui, *ACS Nano* **2011**, *5*, 8346.
[24] L. B. Hu, H. Wu, Y. F. Gao, A. Y. Cao, H. B. Li, J. McDough, X. Xie, M. Zhou, Y. Cui, *Adv. Energy Mater.* **2011**, *1*, 523.
[25] P. C. Lian, X. F. Zhu, S. Z. Liang, Z. Li, W. S. Yang, *Electrochim. Acta* **2011**, *56*, 4532.
[26] X. J. Zhu, Y. W. Zhu, S. Murali, M. D. Stoller, R. S. Ruoff, *J. Power Sources* **2011**, *196*, 6473.
[27] J. Lin, Z. Peng, C. Xiang, G. Ruan, Z. Yan, D. Natelson, J. M. Tour, *ACS Nano* **2013**, *7*, 6001.
[28] Y. Y. Hu, Z. Liu, K. W. Nam, O. J. Borkiewicz, J. Cheng, X. Hua, M. T. Dunstan, X. Yu, K. M. Wiaderek, L. Du, K. W. Chapman, P. J. Chupas, X. Q. Yang, C. P. Grey, *Nat. Mater.* **2013**, doi:10.1038/nmat3784.
[29] Y. F. Shi, B. K. Guo, S. A. Corr, Q. H. Shi, Y. S. Hu, K. R. Heier, L. Q. Chen, R. Seshadri, G. D. Stucky, *Nano Lett.* **2009**, *9*, 4215.
[30] M. Pernet, P. Strobel, B. Bonnet, P. Bordet, Y. Chabre, *Solid State Ionics* **1993**, *66*, 259.